Low-frequency ultrasound-mediated cytokine transfection enhances T cell recruitment at local and distant tumor sites

Tali Ilovitsh[a,b,c], Yi Feng[a,b,d], Josquin Foiret[a,b], Azadeh Kheirolomoom[a,b,c], Hua Zhang[a,b,c], Elizabeth S. Ingham[c], Asaf Ilovitsh[a,b,c], Spencer K. Tumbale[a,b], Brett Z. Fite[a,b], Bo Wu[a,b], Marina N. Raie[a,b], Nisi Zhang[a,b], Aris J. Kare[a,b,e], Michael Chavez[e], Lei S. Qi[e], Gadi Pelled[f,g], Dan Gazit[f,g], Ophir Vermesh[a,b], Idan Steinberg[a,b], Sanjiv S. Gambhir[a,b], and Katherine W. Ferrara[a,b,1]

[a]Molecular Imaging Program at Stanford, Stanford University, Stanford, CA 94305; [b]Department of Radiology, Stanford University, Stanford, CA 94305; [c]Department of Biomedical Engineering, University of California, Davis, CA 95616; [d]Department of Biomedical Engineering, Xi'an Jiaotong University, Xi'an 710049, People's Republic of China; [e]Department of Bioengineering, Stanford University, Stanford, CA 94305; [f]Department of Surgery, Cedars-Sinai Medical Center, Los Angeles, CA 90048; and [g]Board of Governors Regenerative Medicine Institute, Cedars-Sinai Medical Center, Los Angeles, CA 90048

Edited by Rakesh K. Jain, Massachusetts General Hospital, Boston, MA, and approved April 3, 2020 (received for review August 28, 2019)

Robust cytotoxic T cell infiltration has proven to be difficult to achieve in solid tumors. We set out to develop a flexible protocol to efficiently transfect tumor and stromal cells to produce immune-activating cytokines, and thus enhance T cell infiltration while debulking tumor mass. By combining ultrasound with tumor-targeted microbubbles, membrane pores are created and facilitate a controllable and local transfection. Here, we applied a substantially lower transmission frequency (250 kHz) than applied previously. The resulting microbubble oscillation was significantly enhanced, reaching an effective expansion ratio of 35 for a peak negative pressure of 500 kPa in vitro. Combining low-frequency ultrasound with tumor-targeted microbubbles and a DNA plasmid construct, 20% of tumor cells remained viable, and ∼20% of these remaining cells were transfected with a reporter gene both in vitro and in vivo. The majority of cells transfected in vivo were mucin 1^+/$CD45^-$ tumor cells. Tumor and stromal cells were then transfected with plasmid DNA encoding IFN-β, producing 150 pg/10^6 cells in vitro, a 150-fold increase compared to no-ultrasound or no-plasmid controls and a 50-fold increase compared to treatment with targeted microbubbles and ultrasound (without IFN-β). This enhancement in secretion exceeds previously reported fourfold to fivefold increases with other in vitro treatments. Combined with intraperitoneal administration of checkpoint inhibition, a single application of IFN-β plasmid transfection reduced tumor growth in vivo and recruited efficacious immune cells at both the local and distant tumor sites.

ultrasound | transfection | microbubble

Checkpoint inhibition strategies have been effective in overcoming the inhibitory mechanisms primarily dictated by the PD-1/PD-L1 axis and result in significant clinical responses for a subset of patients (1). Nevertheless, therapeutic efficacy remains limited in tumors lacking a robust T cell infiltration (2). Ultrasound (US)-mediated gene delivery has the potential to transfect tumor and stromal cells with genes encoding for immune-related cytokine and chemokine production, while simultaneously debulking the tumor. US enhances the permeability of surrounding cells, allowing targeted local drug and gene delivery through a method known as sonoporation (3–5). Sonoporation is defined as the use of US to introduce pores in cell membranes. Here, we apply sonoporation to transfect solid tumor cells with plasmid DNA (pDNA) encoding IFN-β to trigger a systemic immune response in directly treated and distant tumors (as illustrated in Fig. 1) and combine this with checkpoint inhibition. IFN-β is associated with the suppression of tumor growth and immune system stimulation through increasing natural killer cell activity, cytotoxic T lymphocyte activity, and T helper cell generation (6).

In vivo gene delivery protocols have been designed to modulate expression, overcome deficiencies, compensate for abnormal expression patterns, or replace a malfunctioning gene (7). Gene therapy is now enhancing survival (8), and over 2,600 gene therapy clinical trials have been completed, are ongoing, or have been approved worldwide (9). Although viral vectors, such as retroviruses and adenoviruses, yield higher transduction efficiency, serious concerns exist regarding their immunogenicity, systemic toxicity, insertional mutagenesis, and limited site specificity (10–12). Nonviral chemical and physical transfection methods have emerged as cost-effective, targeted, and safer alternatives to viral vectors with high potential for clinical translation (13). However, these methods are generally less efficient. Chemical methods often lack selectivity toward target tissues and generate high toxicity (13, 14). Among the physical methods, a widely used procedure is electroporation, where electrical pulses induce transient pore formation in the cell membrane within the target tissue (15). Since the electrodes must be adjacent to the

Significance

While immunotherapy has shown great promise for the treatment of T cell-inflamed tumors, a large fraction of cancer patients has not yet seen the benefit of immunotherapy. Furthermore, many immunotherapy protocols involving the systemic administration of multiple immunomodulatory antibodies create a significant toxicity. The platform technology under development here aims to address the need for local effective and nontoxic therapy by developing a minimally invasive tumor transfection method with minimal off-target toxicity. Local administration of a plasmid and microbubbles, coupled with image-guided low-intensity ultrasound, provides a safe and effective method to create a T cell-inflamed tumor. This technology was used to produce an anticancer cytokine and consequently recruit efficacious immune cells at both the local and distant tumor sites.

Author contributions: T.I., Y.F., J.F., A.K., H.Z., E.S.I., S.K.T., B.Z.F., S.S.G., and K.W.F. designed research; T.I., Y.F., J.F., A.K., H.Z., E.S.I., A.I., S.K.T., B.Z.F., B.W., M.N.R., N.Z., O.V., and I.S. performed research; M.C., L.S.Q., G.P., D.G., O.V., and I.S. contributed new reagents/analytic tools; T.I., H.Z., S.K.T., A.J.K., and K.W.F. analyzed data; and T.I. and K.W.F. wrote the paper.

The authors declare no competing interest.

This article is a PNAS Direct Submission.

Data deposition: All data and scripts reported in this paper have been deposited in Figshare (https://doi.org/10.6084/m9.figshare.12214364.v2).

[1]To whom correspondence may be addressed. Email: kwferrar@stanford.edu.

This article contains supporting information online at https://www.pnas.org/lookup/suppl/doi:10.1073/pnas.1914906117/-/DCSupplemental.

First published May 19, 2020.

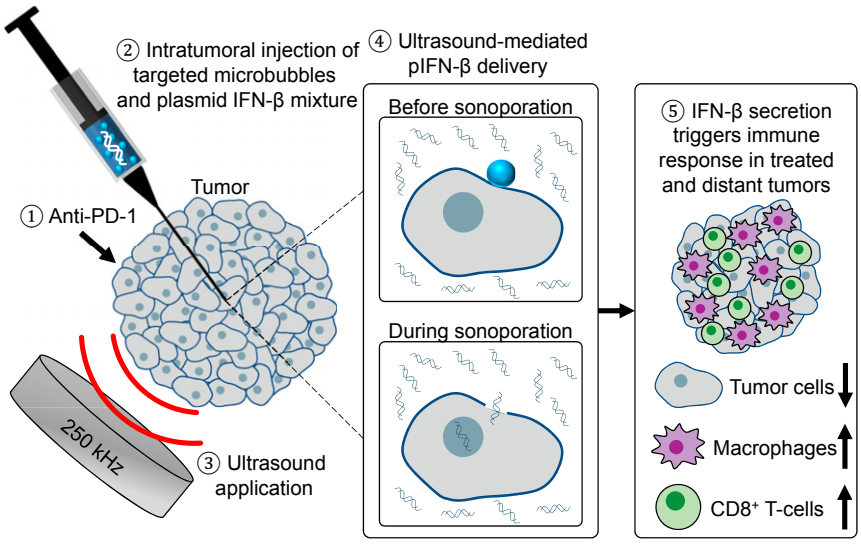

Fig. 1. Schematic illustration of tumor transfection steps of operation (*Left* to *Right*). Syringe and transducer are not drawn to scale. Anti–PD-1 is injected 3 d prior to and 2 d following the US treatment. Targeted microbubbles and plasmid IFN-β (pIFN-β) are mixed and intratumorally injected. Low-frequency US with a center frequency of 250 kHz is then applied to the tumor to facilitate US-mediated pIFN-β delivery. Once the plasmid is transcribed and translated, IFN-β protein is secreted, initiating an immune response in the directly treated and the distant tumors. As a result, the tumor cell population is reduced, while the immune cell population, particularly macrophages and $CD8^+$ T cells, increases.

treated site, the method is limited to shallow targets. Otherwise, this approach requires invasive surgical approaches (16).

Creation of a low-cost, efficient, site-specific, and nontoxic nonviral gene transduction method remains a grand challenge. In recent years, sonoporation has emerged as a promising nonviral delivery method (3–5) and is endowed with the advantages of US (safety, ease of use, cost effectiveness, and clinical availability). Here, microbubble (MB) contrast agents, composed of a gas core and a stabilizing shell, are used to transiently form pores in the cell membrane and facilitate transmembrane transport of drugs and genes (17–19). Following insonation, the cell membrane can restore its integrity, and the delivered material remains trapped within the cell (20). Since US can be applied noninvasively to deep-lying tissues with direct site specificity, deep tissues can be transduced with minimal systemic side effects. Transfection via sonoporation has been employed for delivering genes to numerous organs and tissues, including the brain (21, 22), liver (23), pancreas (24), muscle (25–27), tendon (28), and vasculature (29, 30). Applications include healing bone fracture defects (31, 32), reconstruction of anterior cruciate ligament (33), and hindlimb ischemia (34).

To date, US-mediated tumor transfection remains a particularly difficult challenge (35–37). Some tissues, for example muscle, are tightly structured and known to internalize DNA (38). For these tissues, US peak negative pressures (PNPs) of hundreds of kilopascals can enhance DNA uptake, yielding high cell viability alongside high gene expression. Compared to muscle, tumor transfection efficiency is reduced, since tumors do not uptake DNA autonomously (38). Therefore, higher pressures [on the order of 1 to 10 MPa for a center frequency of 1 to 5 MHz (23, 39–41)] have been proposed, with a resulting modest transfection efficacy of 1 to 5% of live cells. This efficiency is lower than that obtained with electroporation (13, 39, 42). A critical factor in efficient delivery is the size of the pores resulting from insonation relative to the size of the target cargo. In previous reports, real-time observation correlated the PNP with the pore size. At low PNP (below 1 MPa), pore sizes range from tens to 150 nanometers (43, 44). Membrane-impermeant dyes such as propidium iodide and dextran (ranging from 2 to 11 nm, molecular weight of 3 to 500 kDa) (45–47) are well suited for delivery through these pores and are therefore the most common molecules studied in sonoporation. On the other hand, pDNA is often over two orders of magnitude larger [pGFP is 7.5 kbp with an estimated molecular weight of 4.95 MDa and hydrodynamic diameter of ∼350 nm (48)]. Since these plasmids are larger than the typical pores generated by megahertz frequency sonoporation, delivery is anticipated to be inefficient.

The method proposed in this paper uniquely uses low-frequency US (e.g., a center frequency of 250 kHz) to enhance the pore size and combines this with an intratumoral (IT) injection of cell-targeted MBs (TMBs) together with pDNA. This kilohertz frequency range has recently entered clinical use for brain therapy applications, since focusing through the human skull can be achieved with reduced distortion and attenuation (49, 50). In the past, it was assumed that MB oscillations are maximized around their resonance frequency (2 to 10 MHz) (51–54). Recently, we showed that when MBs are excited by a frequency of 250 kHz (an order of magnitude below the resonance frequency of these agents), their oscillations reach an expansion ratio of 35 at a relatively low PNP of 500 kPa (55). For tumor transfection, we hypothesize that the high-amplitude MB oscillations occurring at a center frequency of 250 kHz will enhance the uptake of the genetic material, allowing for more copies to be delivered and resulting in a higher transfection efficacy. The paper is organized as follows. First, ultrahigh-speed optical imaging was used to directly observe MBs targeted to cancer cells and insonated at 250 kHz in vitro. Next, the proposed transfection method was optimized in a suspension of cultured cancer cells through the delivery of a plasmid encoding GFP (pGFP) or IFN-β (pIFN-β). Subsequently, in vivo transfection of murine breast cancer with optical reporter genes (plasmid luciferase [pLUC] and pGFP) was carried out with the optimized in vitro parameters. Last, checkpoint inhibition was combined with pIFN-β transfection to effectively recruit T cells at local and distant tumor sites.

Results

Ultrahigh-Speed Imaging Results. We first confirmed the enhanced collapse velocity obtained with the lower US center frequency through simulation. Both the MB expansion (defined as the ratio

between the peak MB diameter and MB diameter without US) and collapse velocity were enhanced when excited with an US frequency of 250 kHz compared to a higher frequency (*SI Appendix*, Fig. S1). For the 250-kHz frequency, the wall velocity on collapse reached thousands of meters per second for an US pressure exceeding 200 kPa.

The close proximity between the MBs and the cell membrane is known to play a significant role in membrane perforation (44). Therefore, in this study, TMBs, bound directly to the cell membrane, were employed and initially compared to free MBs (FMBs). In the past, the oscillations of TMBs were reported to be dampened when bound to rigid surfaces and excited with a megahertz frequency (56–58). With an ultrahigh-speed camera, we experimentally tested whether TMBs bound to human lung adenocarcinoma (HCC827) cells exhibit dampened oscillation (Fig. 2*A*). We chose a TMB concentration such that, on average, each cell was labeled with a single TMB. Conventional optical imaging first confirmed that bound TMBs (Fig. 2*B*) were destroyed following an US pulse at a PNP of 190 kPa (Fig. 2*C*). Ultrahigh-speed images of ∼180 oscillating MBs were then individually processed to measure the diameter as a function of time at various PNPs (examples in Fig. 2 *D*–*F*). With a PNP of 130 kPa, cavitation was stable, as evidenced by the intact MB after insonation (Fig. 2*D*). The crossover from stable to inertial cavitation occurred below a PNP of 190 kPa and resulted in MB fragmentation (Fig. 2*E*).

The TMBs oscillated asymmetrically in the plane normal to the cell boundary, such that the expansion ratio and the wall velocity at the MB's free (nonadherent) side was increased relative to the adherent surface and relative to FMB oscillation. For each image, the TMB expansion ratio in the image plane was calculated as follows:

$$\text{Expansion ratio} = \frac{W_1 + W_2}{2R_0}, \qquad [1]$$

where R_0 is the resting MB radius, W_1 is the expansion of the MB's adherent side, and W_2 is the expansion of the MB's free side (as indicated in Fig. 2*F*). W_1 and W_2 are measured at the point of maximal expansion. With 250-kPa insonation, the effective expansion ratio was 11 and was followed by fragmentation; however, clearly, the free wall expansion was larger (Fig. 2*F*). For the same PNP of 230 kPa, the radial oscillations of FMBs are symmetrical ($W_2 = W_1$) (Fig. 2*G*), whereas oscillations of TMBs were asymmetrical (i.e., $W_2 > W_1$) (Fig. 2*H*). Next, we evaluated the expansion ratio, W_1, and W_2 for FMBs and TMBs as a function of PNP (Fig. 2*I*). While the average measured expansion ratios for both the FMB and TMB (Av TMB in Fig. 2 *G*–*I*) were similar, expansion was greater at the TMB free wall (W_2) than at its cell membrane-bound wall (W_1). Therefore, the expansion ratio of W_2 (defined as W_2/R_0) was substantially greater than the average or that of W_1. The expansion ratio increases nonlinearly, reaching 45 for W_2 at 430 kPa for TMBs with a resting radius of 0.75 μm. The asymmetry factor, defined as W_2/W_1, also increased with PNP (Fig. 2*I*) and reached 3.5 at 430 kPa (*SI Appendix*, Fig. S2). While MB expansion is relatively slow and therefore easily quantified, collapse is much more rapid and is

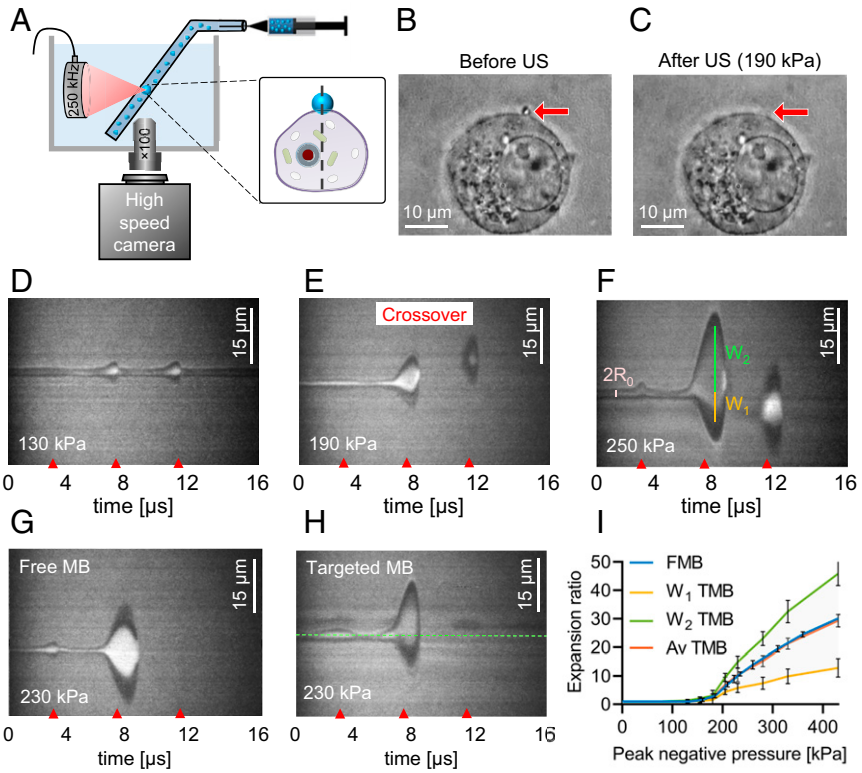

Fig. 2. Ultrahigh-speed imaging of oscillating targeted microbubbles (TMBs) adherent to cells at a transmission center frequency of 250 kHz. (*A*) Ultrahigh-speed imaging setup. TMBs presented in this figure are adherent to the top of the cells. A two-dimensional image of a cell with a single TMB adherent to its top (indicated by a red arrow): (*B*) prior to the transmission of an ultrasound (US) pulse and (*C*) following transmission of an US pulse with a peak negative pressure (PNP) of 190 kPa, at which the TMB was destroyed. Streak images of oscillating TMBs adherent to cells at various PNPs: (*D*) 130 kPa (stable cavitation), (*E*) 190 kPa (crossover to inertial cavitation), and (*F*) 250 kPa (inertial cavitation). R_0 indicates the MB resting radius (here 0.75 μm), and W_1 and W_2 are the maximal expansion of the MB's adherent and free sides, respectively. Streak images for a PNP of 230 kPa for (*G*) free MB (FMB) and (*H*) TMBs. (*I*) Expansion ratio as a function of PNP for FMBs, bound (W_1) and free (W_2) walls of TMBs, and average (Av) expansion ratio of TMBs ($n = 3$ at each PNP). All data are plotted as mean ± SD.

difficult to quantify even with ultrahigh-speed photography. However, we observe that the unbound wall collapse of a TMB was significantly more rapid than that achieved by a FMB (given that the wall travels a greater distance in the same time period) and the velocity approaches the theoretical prediction of thousands of meters per second from *SI Appendix*, Fig. S1.

In Vitro Transfection Results. In vitro transfection experiments were conducted for cells in suspension, using a custom-made experimental system (illustrated in Fig. 3*A*). Initial transfection experiments were carried out with HCC827 cells, and pGFP was delivered via sonoporation at a center frequency of 250 kHz. Five days following the US treatment, the percentage of GFP^+ cells was quantified using flow cytometry (Fig. 3*B*). For the samples treated with US + TMB + pGFP, the percentage of live cells that were transfected increased as a function of the PNP, reaching ~33% of live cells at a PNP of 500 kPa. With a constant fluorescence threshold, the fraction of GFP^+ live cells was greater with 500 kPa, compared to 200-kPa insonation (18.5%; $P < 0.0001$) or control treatments (<6%; $P < 0.0001$) (Fig. 3*B*). Conversely, in all samples treated with US + FMB (rather than TMBs) + pGFP, the GFP signal was similar to that of GFP-only and US + pGFP treatments, and remained below 6% of live cells. Alternatively, with US + TMB + pGFP treatment, cell viability was reduced to ~20% at a PNP of 500 kPa (Fig. 3*C*, $P < 0.0001$). On fluorescence microscopy, GFP was not detected with the FMB-sonoporated sample (Fig. 3 *D* and *E*) but was detected with TMB-sonoporated samples using the same parameters (Fig. 3 *F* and *G*).

After establishing reproducible transfection with the HCC827 cell line, we repeated transfection studies with the neu deletion (NDL) cell line, a syngeneic murine $HER2^+$ orthotopic mammary carcinoma model. With US + TMB + pGFP treatment, similar transfection and viability trends were detected with the NDL cells, i.e., the transfection efficiency increased as a function of the PNP, and the viability decreased. The percentage of GFP^+ live cells was greatest 2 d posttreatment (compared to 1 or 5 d), and greater than that resulting from GFP-only or US + FMB + pGFP control treatments (<7%; $P < 0.0001$) (Fig. 3*H*). Therefore, further in vitro assays were conducted 2 d post-US treatment. For a

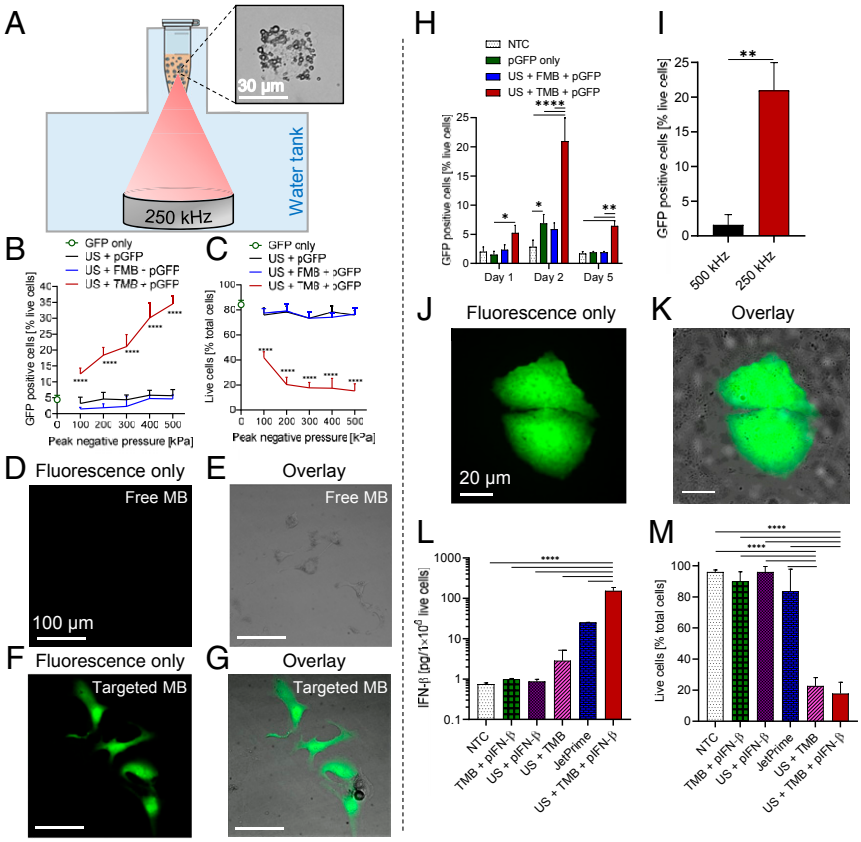

Fig. 3. In vitro transfection of (*B*–*G*) human lung adenocarcinoma (HCC827) and (*H*–*M*) Neu deletion (NDL) metastatic mammary carcinoma cell lines. (*A*) In vitro transfection setup for cells in suspension. Magnified image of a tumor cell with adherent targeted microbubbles (TMBs). (*B*) Flow-cytometric analysis of GFP^+ cells as a function of the peak negative pressure (PNP) 5 d following sonoporation for pGFP only, US + pGFP, US + FMB + pGFP, and US + TMB + pGFP. (*C*) Cell viability as a function of PNP 5 d following sonoporation. (*B* and *C*) Two-way ANOVA for PNP of 100 to 500 kPa with Tukey's multiple-comparisons test. Significance represents US + TMB + pGFP compared to both US + pGFP and US + FMB + pGFP at each pressure. (*D*–*G*) Fluorescence microscopy images of tumor cells 5 d following sonoporation with FMBs and TMBs. (Scale bars: each 100 μm.) (*D*) Fluorescence only for FMB and (*E*) fluorescence and brightfield overlay for FMB. (*F*) Fluorescence only for TMB-treated cells and (*G*) corresponding overlay. (*H*) Flow-cytometric analysis of GFP^+ NDL cells 1, 2, and 5 d post sonoporation with pGFP for no-treatment control (NTC), pGFP only, US + FMB + pGFP, and US + TMB + pGFP. Two-way ANOVA with Tukey's multiple-comparisons test. (*I*) Percentage of GFP^+ cells 2 d post sonoporation using two ultrasound (US) center frequencies (500 and 250 kHz) and PNP of 500 kPa. Welch's *t* test. (*J* and *K*) Fluorescence microscopy images of NDL cells 2 d post sonoporation with TMBs. (*J*) Fluorescence only and (*K*) overlay. (*L*) IFN-β secretion from NDL cells 2 d posttreatment for TMB + pIFN-β (no US), US + pIFN-β (no TMBs), US + TMB (no pIFN- β), JetPrime transfection reagent (positive control), and US + TMB + IFN-β. (*M*) NDL cell viability 2 d posttreatment for NTC, TMB + pIFN-β, US + pIFN-β, JetPrime transfection reagent (positive control), US + TMB, and US + TMB + IFN-β treatment groups. (*L* and *M*) One-way ANOVA with Tukey's multiple-comparisons test. Adjusted *P* values were $*P < 0.05$, $**P < 0.01$, $***P < 0.001$, and $****P < 0.0001$. All data are plotted as mean ± SD.

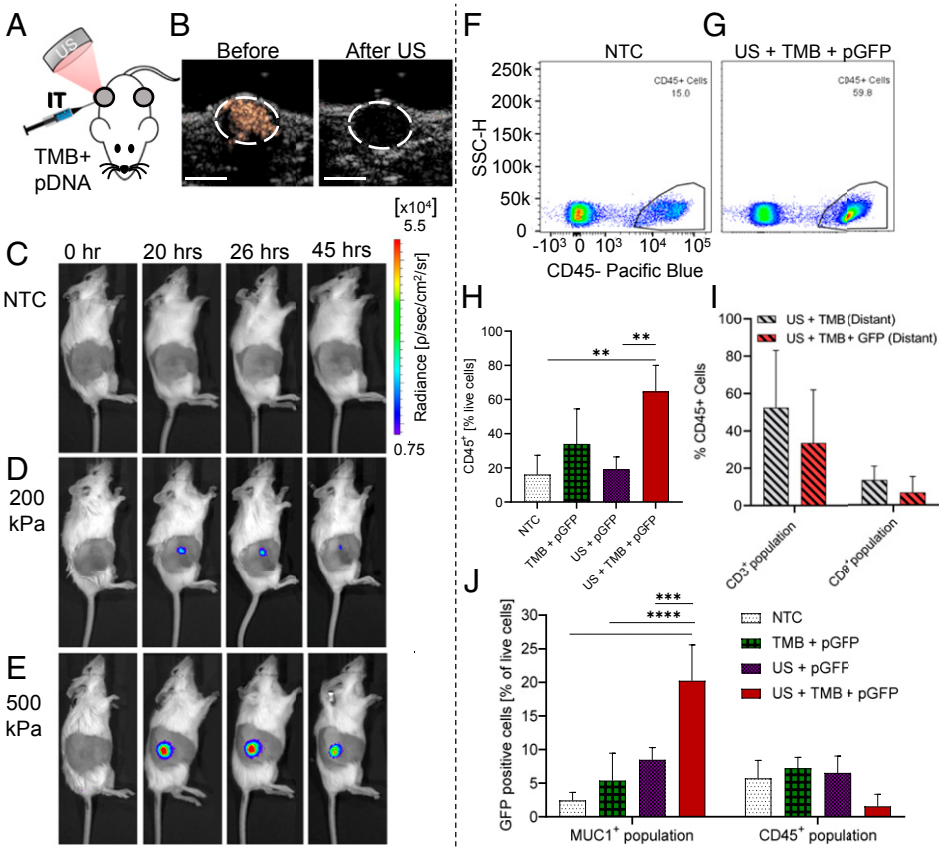

Fig. 4. In vivo optical reporter gene transfection using pLUC and pGFP. (*A*) Mixture of pDNA and targeted microbubbles (TMBs) were intratumorally (IT) injected into one tumor within the bilateral neu deletion (NDL) tumor model in mice, followed by ultrasound (US) application. (*B*) Following the IT injection, contrast pulse sequence US imaging confirmed TMB distribution before therapeutic US (gold overlay) and destruction after therapeutic US. (Scale bar: 2 mm.) (*C*–*E*) Bioluminescence imaging at four time points (0, 20, 26, and 45 h) following pLUC transfection for (*C*) NTC, (*D*) pLUC + TMB + US with a PNP of 200 kPa, and (*E*) pLUC + TMB + US with a PNP of 500 kPa. (*F*–*J*) In vivo flow cytometry results 3 d post pGFP transfection. (*F* and *G*) Representative flow cytometry dot plots illustrating enhanced $CD45^+$ cell recruitment in the (*G*) US + TMB + pGFP–treated tumors compared to (*F*) NTC tumors ($CD45^+$ frequencies are the percentage of the live-cell parent population). (*H*) Frequency of $CD45^+$ cells given as a percentage of live cells. (*I*) Frequency of $CD3^+$ T and $CD8^+$ T cells in the distant tumors given as a percentage of the $CD45^+$ population. (*H* and *I*) One-way ANOVA. (*J*) GFP^+ cells in the $MUC1^+$ versus $CD45^+$ populations. Two-way ANOVA. All comparisons use Tukey's multiple-comparisons test with adjusted *P* values of $^{**}P < 0.01$, $^{***}P < 0.001$, and $^{****}P < 0.0001$. All data are plotted as mean ± SD.

given PNP, reducing the US center frequency from 500 kHz (~1% in vitro transfection) to 250 kHz (~21% in vitro transfection) enhanced transfection efficiency (Fig. 3*I*; $P < 0.01$). Similar to the results obtained with HCC827, the GFP signal was enhanced above baseline in the TMB-sonoporated samples using the center frequency of 250 kHz (Fig. 3 *J* and *K*). pGFP transfection efficiency was similar for no-treatment control (NTC)-treated cells and cells treated in vitro with US + FMB + free CD326 EpCAM antibody + pGFP (*SI Appendix*, Fig. S3), confirming that conjugation of the antibody to the MBs is required to enhance transfection.

After successfully transfecting the NDL cell line with a GFP reporter gene, we sought to deliver pIFN-β in vitro and evaluated IFN-β secretion via enzyme-linked immunosorbent assay (ELISA). The same US parameters that were successful for pGFP delivery yielded significant enhancement of IFN-β secretion in the TMB-sonoporated samples, reaching an average of 153 pg of IFN-β per 10^6 live cells. This represents a 150-fold increase compared to NTC, TMB + pIFN-β (no US), and US + pIFN-β (no TMB) groups (<1 pg per 10^6 live cells on average; $P < 0.0001$) and a 6-fold increase compared to a common lipid-based transfection reagent (JetPrime) positive control (25 pg per 10^6 live cells; $P < 0.0001$) (Fig. 3*L*). US + TMB alone increased IFN-β secretion to 3 pg per 10^6 live cells. The viability was ~83% for the JetPrime samples and decreased to ~20% for the TMB-sonoporated samples (with or without plasmid; $P < 0.0001$) (Fig. 3*M*). NDL cell viability was similar between the NTC, TMB + pIFN-β (no US), and US + pIFN-β (no TMB) samples.

In Vivo Reporter Gene Transfection Results. In vivo transfection experiments were performed in the bilateral NDL murine breast cancer model, using plasmids encoding optical reporter genes (pLUC and pGFP) and a therapeutic cytokine (pIFN-β). The delivery of pLUC enabled in vivo direct visualization via bioluminescence imaging while pGFP facilitated quantitation of transfection on a per-cell basis using flow cytometry. Last, the delivery of pIFN-β was combined with checkpoint inhibition, and response evaluated using tumor growth rate, immunohistochemistry (IHC), flow cytometry, ELISA, and a survival study. Plasmid delivery via sonoporation was carried out by IT injection of a mixture of TMBs with pDNA (injected volume was below 25 μL) into one tumor within the bilateral model (Fig. 4*A*). Following IT injection, wide tumor distribution of TMBs was visualized with contrast pulse sequence nonlinear imaging (gold overlay) (Fig. 4*B*). Three-dimensional imaging further confirmed the TMB distribution through the tumor (*SI Appendix*, Fig. S4). Following therapeutic US delivery using the in vitro optimized parameters, US imaging confirmed the destruction of TMBs inside the tumor (Fig. 4*B*).

Bioluminescence imaging at four time points (0, 20, 26, and 45 h) tracked luciferase gene expression. Expression was greatest between 20 and 26 h after insonation (*SI Appendix*, Fig. S5*A*). Luciferase expression was absent in NTC mice (Fig. 4*C*), detected in mice treated with pLUC + TMB + US using 200 kPa (Fig. 4*D*), and enhanced fivefold further in mice treated with 500 kPa (compared with 200 kPa [$P < 0.01$]) (Fig. 4*E* and *SI Appendix*, Fig. S5*A*). Compared to the 26-h time point, the total flux was on average reduced by 45 h (*SI Appendix*, Fig. S5*A*). At 45 h posttreatment, the flux observed with antibody-conjugated MBs was 4.5 times higher compared with peptide-conjugated MBs (targeted to nucleolin) (*SI Appendix*, Fig. S5*B*).

We next transfected the tumors with a GFP reporter gene. The maximal pGFP transgene expression level was expected to be highest on days 2 to 3 (38). Similar to the in vitro studies, the percentage of GFP^+ tumor cells in vivo was ∼6% for day 1 and increased to ∼20% for days 2 ($P < 0.05$) and 3 ($P < 0.01$) (*SI Appendix*, Fig. S5*C*). As assessed by flow cytometry, the frequency of $CD45^+$ cells increased from ∼18% in the NTC (Fig. 4 *F* and *H*) to ∼60% in the samples directly treated with US + TMB + pGFP (Fig. 4 *G* and *H*) ($P < 0.01$). Within the $CD45^+$ cell population in the distant tumors treated with US + TMB and US + TMB + pGFP, the frequency of $CD3^+$ and $CD8^+$ T cells was not significantly different (Fig. 4*I*). Furthermore, IHC obtained 3 d post-US treatment indicated similar macrophage and $CD8^+$ T cell numbers between US + TMB and US + TMB + pGFP cohorts (*SI Appendix*, Fig. S6).

The GFP^+ cell percentage in the mucin 1^+ ($MUC1^+$) tumor cell population was ∼20% ($P < 0.0001$), compared to 2.8%, 5.3%, and 6.1% for the NTC, TMB + pGFP, and US + pGFP control cohorts, respectively (Fig. 4*J*). An inverse trend was observed for the $CD45^+$ cell population, where the GFP^+ cell percentage in the control treatments was ∼6% and reduced to 1.6% for the US + TMB + pGFP treatment (Fig. 4*J*). This reduction was expected since leukocytes infiltrated after treatment. The GFP signal was not significantly increased above baseline in the absence of US or TMBs (Fig. 4*J*).

In Vivo Cavitation and Temperature and Impact on Tumor Viability. Passive cavitation detection was used to monitor the in vivo cavitation activity by recording and quantifying ultraharmonic components and broadband energy in the spectrum. Ultraharmonics were detected in the spectrum for up to 20 s during US application (*SI Appendix*, Fig. S7 *A*–*C*). At later time points, ultraharmonics diminish suggesting TMB destruction. Temperature monitoring during the treatment indicated a maximal temperature increase of an average of 2.5 ± 1.2 °C (*SI Appendix*, Fig. S7*D*); however, the tumor temperature was slightly reduced at the time of treatment onset. Therefore, the tumors did not become hyperthermic (maximal temperature was below 37 °C).

Furthermore, to prove that the high-amplitude TMB oscillations are capable of debulking the tumor and reducing its viability, IHC 2 d posttreatment assessed tumor viability and near-term immune response (Fig. 5). Extensive damage and reduced tumor viability were visualized with hematoxylin and eosin (H&E) staining, indicating that large MB oscillation occurred in the center of tumors treated with US + TMB + pGFP. IHC also confirmed macrophage infiltration within the treated tumors in the damaged regions; however, $CD8^+$ T cell infiltration was not significantly enhanced (Fig. 5). By comparison, tumors treated with nontargeted FMBs or with biotin-streptavidin MBs did not exhibit similar tumor damage or macrophage and $CD8^+$ T cell infiltration (*SI Appendix*, Fig. S8).

In Vivo Therapeutic Cytokine Gene Transfection Results. The pGFP transfection results suggest that the treatment reduces tumor viability and recruits immune cells. We sought to further enhance and amplify the immune response and generate a systemic immune response by transfecting the tumor with pIFN-β. Since the tumor's checkpoint inhibitory mechanisms limit immune cell activity, the transfection protocol incorporated the administration of an anti–PD-1 (aPD-1) checkpoint inhibitor. Initially, aPD-1 was administered 3 d prior to the pIFN-β transfection, and the tumors and blood were collected 2 d post sonoporation and assayed using ELISA and flow cytometry (full regimen is presented in *SI Appendix*, Fig. S9*A*). In the directly treated tumors, IFN-β secretion levels in the remaining tumor rim were significantly increased, reaching 3.8 pg/mg of protein compared to 1.1 pg/mg in the NTC ($P < 0.001$) (*SI Appendix*, Fig. S9*B*). IFN-β levels in the plasma were not elevated compared to the other cohorts for this time point; however, the frequency of $CD45^+$ cells in the blood was increased compared to NTC ($P < 0.05$), reaching 48% of live cells for the US + TMB + pIFN-β + aPD-1 samples, compared to 25% and 31% for the NTC and aPD-1-only groups, respectively (*SI Appendix*, Fig. S9*C*).

For ablative treatments in refs. 59 and 60, T cell infiltration in distant tumors was enhanced a week following US ablation, and therefore we chose this time point to evaluate the T cell infiltration. Here, aPD-1 was administered 3 d prior to and 2 d

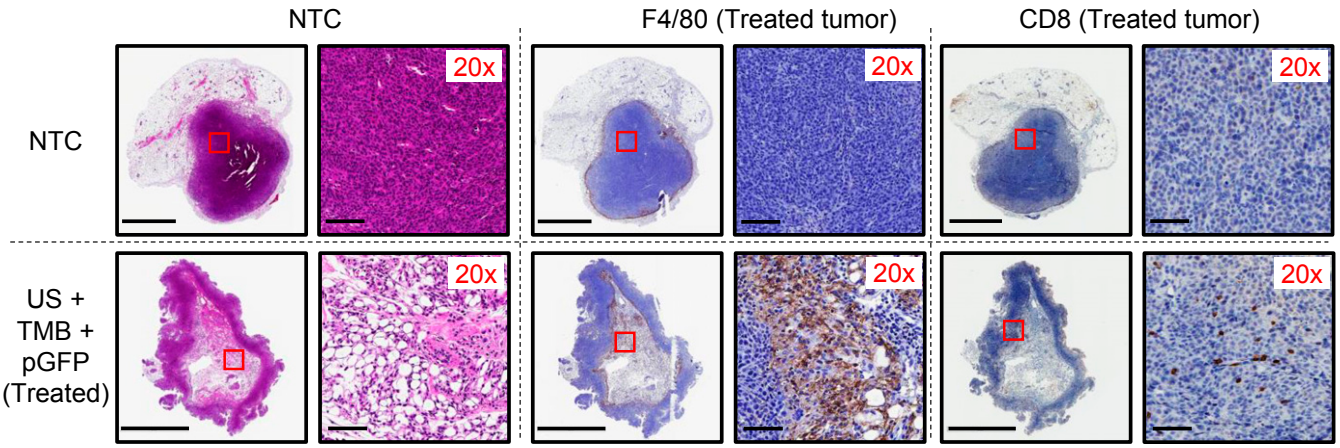

Fig. 5. IHC (H&E, F4/80, and CD8 staining) 2 d post pGFP transfection in no-treatment control (NTC) and directly treated US + TMB + pGFP tumors. (Scale bars: 2 mm for tumor cross-sections; 100 μm for 20× images.)

following pIFN-β transfection with sonoporation (full regimen is presented in Fig. 6*A*). On IHC gathered 7 d post sonoporation (~21 d post cell injection), immune cell infiltration ($F4/80^+$ macrophages and $CD8^+$ T cells) was increased in both the directly treated tumors and the distant tumors, compared to all other controls (Fig. 6 *B–D* and *SI Appendix*, Fig. S10). The frequency of tumor-infiltrating $F4/80^+$ macrophages (Fig. 6*C*) and $CD8^+$ T cells (Fig. 6*D*) was quantified at 7 d following treatment. $F4/80^+$ macrophages were enhanced in the directly treated tumor with US + TMB + pIFN-β + aPD-1 treatment; ~18% of cells were macrophages, an increase of 6.5-, 4-, and 2.5-fold compared to NTC, aPD-1–only, and US + TMB–only groups, respectively ($P < 0.0001$). The effect on the distant tumor is also pronounced, with macrophages representing ~8.5% of the cells in the distant tumor following treatment with US + TMB + pIFN-β + aPD-1, a 3.1-, 1.8-, and 2.14-fold increase compared to the NTC, aPD-1, and US + TMB–only groups, respectively (Fig. 6*C*). T cell recruitment in the directly treated tumors also increased 7-, 4.2-, and 3-fold compared to the NTC, aPD-1 only, and US + TMB–only treatment groups, respectively ($P < 0.0001$, Fig. 6*D*). Distant tumor T cell recruitment was enhanced 3.4-, 2-, and 2.5-fold compared to the NTC ($P < 0.01$), aPD-1 ($P < 0.05$), and US + TMB distant tumors (with or without plasmid) groups, respectively ($P < 0.01$, Fig. 6*D*). For the US + TMB protocol (without pIFN-β), T cell recruitment was enhanced only in the directly treated tumors (2.5-fold compared to NTC; $P < 0.05$). Immune cell recruitment was similar (and reduced) in tumors treated with US + TMB + pIFN-β (without aPD-1), US + TMB + aPD-1 (without plasmid), and US + TMB (*SI Appendix*, Fig. S10).

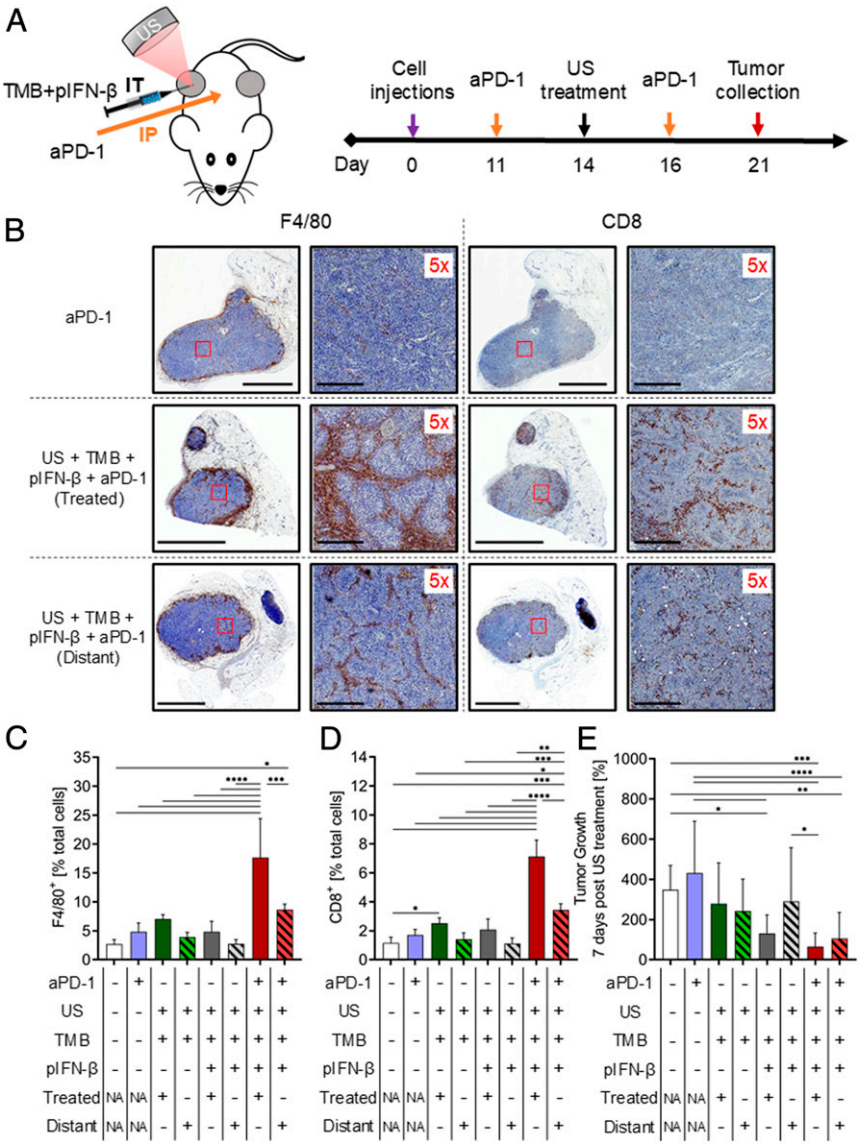

Fig. 6. pIFN-β transfection triggers immune infiltration in directly treated and distant tumors. (*A*) Regimen of pIFN-β transfection for evaluating immune response 1 wk following sonoporation. (*B*) $CD8^+$ T and $F4/80^+$ cell (brown overlay) infiltration increased in both treated and distant tumors following treatment with US + TMB + pIFN-β + aPD-1 compared to administration of aPD-1 alone. (Scale bars: 3 mm for tumor cross-sections; 500 μm for 5× images.) (*C*) Frequency of macrophages ($F4/80^+$ cells), given as a percentage of total cells, quantified from IHC images. (*D*) Frequency of $CD8^+$ T cells, given as a percentage of total cells, quantified from IHC images. (*C* and *D*) One-way ANOVA with Tukey's multiple-comparisons test. (*E*) NDL tumor growth for the various treatments on day 7 post US treatment. (One-way ANOVA with Fisher's least significant difference test.) $^*P < 0.05$, $^{**}P < 0.01$, $^{***}P < 0.001$, and $^{****}P < 0.0001$. All data are plotted as mean ± SD.

T cell activation, assessed via OX40 staining, increased in directly treated and distant tumors and surrounding lymph nodes for mice that received the combined treatment (US + TMB + pIFN-β + aPD-1), compared to all other controls (*SI Appendix*, Figs. S11 and S12). Foxp3 (regulatory T cells) and CD206-expressing cells (assumed to be M2 macrophages) did not increase within the treated and distant tumors (*SI Appendix*, Fig. S13).

Evaluated on day 7 post-US treatment, tumor growth reduction was greatest in treated and distant tumors following the full US + TMB + pIFN-β + aPD-1 treatment, compared to control (partial) treatments (Fig. 6*E*). Tumor volume was reduced 1 wk after the first US + TMB + pIFN-β + aPD-1 treatment (*SI Appendix*, Fig. S14). The treated and distant tumors were each smaller than the NTC ($P < 0.0001$) and US + TMB + aPD-1–treated cohorts ($P < 0.05$). Moreover, survival was enhanced with US + TMB + pIFN-β + aPD-1 compared to all of the other cohorts ($P < 0.05$) (*SI Appendix*, Fig. S15). Only in the combined treatment group was complete regression attained as one of six mice had no detectable tumors in the treated or distant site at day 70.

Discussion

Our central goal in this work was to develop an US-based platform technology for combining tumor debulking with effective and reproducible transfection. Since the ratio of immune cells to tumor burden is known to play a critical role in T cell-mediated therapy (1), reduction in tumor bulk combined with enhanced T cell infiltration is particularly attractive. We believe that such a minimally invasive and easily repeated treatment can find a place in the arsenal of immunotherapy protocols. Therapeutic applications of US have expanded to include most major organ sites, and tumors can be debulked through US-mediated cavitation or thermal ablation. Here, cavitation resulting from insonation of TMBs reduced viability while transfecting tumor cells. There are two major differences compared to previous work. First, by using a lower frequency than previous studies, the fraction of cells transfected and the expression levels of the transfected cytokine were enhanced (61, 62). In vitro secretion of IFN-β reached 150 pg/10^6 cells for the remaining viable tumor cells, a 150-fold increase compared to no-US or no-plasmid controls and a 50-fold increase compared to treatment with TMBs and US (without IFN-β). This result exceeds values of fourfold to fivefold improvement reported for ablative, radiotherapy, and chemotherapeutic treatments in previous in vitro studies (60, 63, 64). Second, by incorporating a checkpoint inhibitor, we were able to enhance T cell recruitment as a result of sonoporation.

Successful US-mediated transfection requires the carefully controlled protocol components elucidated here: creation and titration of antibody-targeted MBs for both in vitro and in vivo application, selection of US parameters (frequency, pressure, and duration), control of plasmid dose and concentration, and real-time control of insonation through cavitation detection and imaging. We confirmed that TMB oscillations are enhanced upon 250-kHz insonation, and these high-amplitude oscillations facilitate gene delivery and tumor debulking. As a result of the cavitation-mediated debulking and transfection, immune cells ($CD8^+$ T cells and macrophages) infiltrated the center of both the directly treated and distant tumors.

Such nonviral US-mediated gene therapy holds promise for clinical translation (9) due to 1) the reduced immunogenicity and risk of insertional mutagenesis compared to viral methods (13) and 2) minimal invasiveness compared to physical approaches such as electroporation. Thus, it is generally accepted that nonviral vectors have greater potential for clinical translation. While gene therapy via sonoporation has previously been successfully applied to various tissues and organs (21–30), efforts to efficiently transfect tumors are ongoing (35–37). To date, a relatively low transfection efficiency has been achieved with US compared to the aforementioned methods (13). The protocol developed here is generally applicable, facilitating the introduction of a wide range of cytokines and chemokines into tumor and stromal cells, as well as a variety of other plasmid types. When combined with checkpoint inhibition, T cell recruitment was enhanced at both the local and distant sites.

We selected IFN-β as the therapeutic plasmid due to hypothesized synergy with the combined TMB and US treatment. Inertial cavitation, as performed here, results in mechanical damage to surrounding cells, releases nucleic acids, and has the potential to induce both damage and pathogen-associated molecular profiles (65). Such damage also results in the production of type 1 IFN by cells including lymphocytes (NK cells, B cells, and T cells), macrophages, fibroblasts, and endothelial cells. Thus, we anticipated and confirmed a low level of IFN secretion in the absence of the plasmid. Still, IFN production, immune cell recruitment, and survival were enhanced by the combined treatment, compared with the TMB + US treatment alone.

Impact of Low-Frequency Oscillation. The use of low-frequency US enlarges the focal zone and increases the penetration depth, enabling the treatment of extensive and deep-lying tumors. TMB oscillations were enhanced with 250-kHz insonation (compared with higher frequencies) as observed using ultrahigh-speed imaging. Using passive cavitation detection, inertial cavitation activity (and thus intense oscillation) was also confirmed within tumors when TMBs were insonated at 250 kHz. IHC further confirmed tumor debulking as a result of this inertial cavitation. Previously, we applied ultrafast optical imaging of MBs in very small vessels to directly visualize in vivo MB oscillation (66). Upon megahertz insonation, while MB expansion was constrained in small vessels, rapid collapse into the endothelium did occur and MBs jetted into and across the basement membrane. Here, we directly injected TMBs and plasmid in the tumor, and thus the MBs collapse against tumor and stromal cells. Due to the enhanced oscillations at 250 kHz (compared with 1 MHz), these effects are amplified here.

The delivery of large molecules is regulated by induction of endocytosis and pore formation, and this process is hypothesized to be enhanced by the lower US frequency (47). Transfection efficiency increased with increased PNP and reduced center frequency, while cell viability decreased. Therefore, it can be hypothesized that the delivery of pDNA complexes was more efficient when large pores were formed through high-amplitude oscillations of TMBs. Here, a PNP of 500 kPa yielded over 20% transfection in two distinct cell lines, with cell viability of ∼20%. For example, transfection efficacy in the HCC827 cell line was 33% of live cells. Given the 20% cell viability, this translates to a 7% transfection efficacy for all cells. Increasing the PNP is likely to further increase transfection efficiency and reduce cell viability. Therefore, in our study, we focused on a PNP of 500 kPa. Applying the same PNP with a higher center frequency of 500 kHz resulted in ∼1% transfection.

The majority of cells transfected in vivo were $MUC1^+/CD45^-$. Thus, we are not transfecting immune cells directly but instead are enhancing their recruitment. A single application of tumor cell transfection with the type 1 IFN-β plasmid reduced tumor growth and recruited $CD8^+$ T cells, increasing their proportion to ∼7 and 3.5% of cells for the directly treated and distant tumors respectively, compared with 1.1 and 1.7% for NTC and checkpoint inhibition alone. The PNP required and transfection efficiency achieved for the GFP reporter gene was consistent between the in vitro and in vivo experiments, with ∼20% of cells transfected. Since in vitro transfection assays are considered a

prerequisite step for optimizing the experimental conditions, this consistency is important and is facilitated by using the low frequency of 250 kHz. Studies using a higher center frequency have reported that in vivo transfection was accomplished with a higher PNP compared with in vitro transfection (30, 45).

In our study, we chose to focus on the delivery of pDNA complexes. In order to transfect, plasmids are transported into the nucleus, a process that requires several days. The maximal pGFP transgene expression level was highest on days 2 and 3, in agreement with what was reported in ref. 38.

Impact of Molecular Targeting. The in vitro comparison of the transfection efficacy using FMBs and TMBs suggests that the proximity of the MBs to the cells is a crucial factor required to effectively transfect tumor cells (44). This is achieved using TMBs that adhere to the surface of the cancer cells. Insonation of MBs without biotin–streptavidin (nontargeted FMB) or with biotin–streptavidin without the antibody did not produce tissue damage or macrophage and $CD8^+$ T cell infiltration. This is in agreement with other studies that report that streptavidin and biotin alone are well tolerated and do not trigger immunogenic events (67). The CD326 antibody alone did not produce a significant therapeutic effect in numerous clinical trials in ref. 68 or in our work when coinjected with FMBs as a component of the treatment. Here, insonation of TMBs was insufficient to produce comparable immune infiltration. If needed, for future clinical use, other types of conjugation chemistries could be considered such as maleimide-thiol conjugation chemistry (69), or peptide conjugation strategies (70). Here, conjugation of a peptide targeted to nucleolin did not result in similar transfection efficiency as antibody conjugation.

Intratumoral Immunotherapy. In order to achieve a precise concentration of MBs and plasmid at the tumor site, we directly injected these therapeutics into the tumor. Clinical trials of such IT-delivered immunotherapies, where the immunostimulatory agent is injected directly into the tumor rather than systemically, are expanding in number and organ sites (71). Expert clinicians report that sites for which biopsy is feasible can also be injected with the comparatively smaller needles required for therapeutic delivery. With IT injection, we aim to reduce systemic exposure, off-target toxicity, and mass of injected therapeutic, while producing an effective antitumor response in both the injected and distant tumors. In this context, the treatment described here can be applied to most organ sites (72).

Limitations of the Study. There are multiple limitations to this work that should be considered. Our primary goal was to develop and optimize the methodology to debulk tumor and transfect tumor cells in situ in order to enhance the recruitment of activated $CD8^+$ T cells at local and distant sites. Here, we chose to transfect the tumors with a therapeutic plasmid encoding for IFN-β, recognizing that this plasmid is synergistic with the mechanical US treatment applied here. This provides a general platform on which additional protocols can be developed. However, given that combination immunotherapy protocols have often been shown to be even more potent (2), we recognize that in the future, the efficacy of alternate plasmids or combinations of plasmids should be evaluated. For each plasmid or combination, a comprehensive study should be undertaken prior to concluding as to potential efficacy, mechanisms, and survival enhancement. Such a study is currently underway with additional plasmids.

Furthermore, the low-frequency US-mediated transfection applied here has broad effects on innate and adaptive immune cells, cytokines, angiogenesis, and stromal cells. As a result, it is likely that depleting one cell type will not completely abrogate the response. Once an optimized plasmid combination is established, the exact mechanism needs to be dissected in order to determine whether a macrophage or T cell response is required for efficacy.

The incorporation of a plasmid encoding for a reporter gene can also induce an intended immunogenicity (73). In our work, the macrophage and T cell density was not dependent on the presence of the GFP reporter gene expression; however, this must be evaluated in each model and for each reporter. Finally, the presence of an antibody or peptide on the MB surface can impact response and immunogenicity. Here, insonation with a TMB was essential for transfection, and therefore this factor cannot be eliminated. We recognize that downstream signaling by CD326 could also enhance response, and alternate antibodies should be included in future studies. We conclude that the EpCAM-targeted antibody can be used to enhance transfection in the cell lines studied here and CD326 is a reasonable choice and binds to multiple tumors. On its own, the CD326 antibody did not enhance transfection.

Summary. In summary, we report that low-frequency (e.g., 250-kHz) insonation of tumor-targeted MBs resulted in high-amplitude oscillation in vitro and inertial cavitation in vivo. As a result of the enhanced oscillation, tumors were debulked, and with plasmid coinjection, transfection rates increased. Key protocol requirements developed here include the creation and dosing of antibody–TMBs, optimization of insonation frequency and pressure, and validation through real-time monitoring and phenotypic assays. The resulting platform technology facilitated controlled and localized tumor transfection and can be tailored to induce a desired tumor and immune cell phenotype through the selection of a tumor-specific plasmid. We hypothesized and confirmed that tumor transfection with IFN-β enhanced the damage-associated profile resulting from the insonation of TMBs. When combined with checkpoint inhibition, tumor growth was reduced in both the directly treated and distant tumors, and survival was enhanced.

Materials and Methods

Supplemental materials and methods are available in *SI Appendix*.

MB Preparation. FMBs, composed of a phospholipid shell and a perfluorobutane (C_4F_{10}) gas core, were prepared as reported previously (74) and further described in *SI Appendix*. Three types of TMBs were used in the experiments described here. Two formulations used biotin–streptavidin and biotin–antibody conjugation, and the third involved a conjugate between a nucleolin-targeted peptide and the MB. F3-conjugated TMB were prepared as described previously (74) and were used for comparison to the antibody-conjugated TMB in pLUC delivery. The remaining experiments utilized antibody-conjugated TMBs. In the high-speed imaging experiments, commercially available VisualSonics target-ready MBs (FUJIFILM) were used. The commercial TMBs have an average radius of 0.75 μm and were prepared according to the manufacturer's instructions. The remainder of the experiments employed biotin–TMBs made in-house (see *SI Appendix* for full preparation description) (75). US-driven oscillations were similar for the two TMB formulations. Preparation of biotin-streptavidin–coated MBs was similar to that of TMBs, without antibody conjugation; instead, biotin saturated the exposed streptavidin binding sites.

Two antibodies were used in this study in order to assess transfection of human and mouse cells, and the conjugation methodology was identical. For the HCC827 (human) cell line, biotin-conjugated anti-human CD326 (EpCAM) antibody (clone 9C4; BioLegend) was used. For the NDL (mouse) cell line, biotin-conjugated anti-mouse CD326 (EpCAM) antibody was used (clone G8.8; BioLegend). Ten micrograms of the appropriate antibody was added to the avidin-conjugated MB cake and incubated for 25 min at room temperature on a rotator. Following incubation, MBs were purified again to remove excess antibody. The size and concentration of the purified MBs

were measured with a particle counter system (Accusizer 770A; Particle Sizing Systems). Exemplary size distributions are presented in *SI Appendix*, Fig. S16. The MBs were used within 3 h of their preparation.

Ultrahigh-Speed Optical Imaging Setup. The experimental setup (illustrated in Fig. 2*A*) was described previously (55) and further described in *SI Appendix*. Postprocessing of the captured images was performed in Matlab to yield the resting MB radius and expansion ratio.

Cell Culture and Assays. Two tumor cell lines were included in this study (HCC827 human lung adenocarcinoma and NDL syngeneic metastatic mammary carcinoma). NDL originated from the overexpression of the ErbB-2/neu proto-oncogene (76, 77) and was a generous gift from Alexander Borowsky (University of California, Davis, CA). Cell culture and in vitro transfection methods are further described in *SI Appendix*. Following treatment, cells were cultured at 37 °C in a humidified 5% CO_2 incubator until their assay using flow cytometry or ELISA. GFP fluorescence was monitored by imaging of the cell plates with an upright fluorescence microscope (Mikron Instruments) using a 63× or 20× water-immersion objective and FITC filter set. Flow cytometry was conducted at multiple time points following treatment. For the HCC827 cell line, flow cytometry was performed on days 2 and 5. For the NDL cell line, flow cytometry was performed on days 1, 2, and 5. For flow cytometry, cells were collected in 500 μL of TrypLE Express (Thermo Fisher Scientific), and viable cell number was assessed using a hemocytometer with trypan blue dead cell exclusion. GFP expression was measured on a FACScan flow cytometer (BD Biosciences), and data were analyzed using FlowJo vX software (Tree Star). IFN-β production was assayed 48 h posttreatment via ELISA (#42410; PBL Assay Science) following the manufacturer's instructions. IFN-β concentration was normalized to total cell number (live + dead cells, counted via hemocytometer) for each sample. All treatments were analyzed in triplicate.

In Vitro Transfection Studies. The 250-kHz spherically focused single-element transducer (beam parameters in *SI Appendix*, Fig. S17 *A* and *B*) was placed at the bottom of a degassed water tank facing upwards and aligned to focus at a 0.5-mL Eppendorf tube positioned at the focal depth of the transducer (z = 45 mm) (Fig. 3*A*). Negligible attenuation was detected in needle hydrophone pressure measurements acquired in an Eppendorf tube filled with degassed water compared to water alone. For the in vitro assays, two plasmids were used: pGFP and pIFN-β (see *SI Appendix* for plasmid production details). For pGFP transfection, 2×10^5 cells and 9 μg of plasmid were added to each tube, and for pIFN-β transfection, 1×10^6 cells and 25 μg of plasmid were added to each tube. Sonication in all of the studies included US bursts of 4 ms, pulse repetition frequency of 30 Hz, and total treatment of 3 min. For the groups below, five PNPs were tested, ranging between 100 and 500 kPa, at intervals of 100 kPa. pGFP transfection was performed with two cell lines, HCC827 and NDL. For HCC827 pGFP transfection, five groups were tested (n = 6 per group): 1) no-treatment control (NTC), 2) TMB + pGFP (no US), 3) US + pGFP (no TMB), 4) US + FMB + pGFP, and 5) US + TMB + pGFP. For the NDL pGFP transfection, five groups were tested (n = 6 per group): 1) NTC, 2) pGFP only (no US), 3) US + FMB + pGFP, 4) US + FMB + EpCAM + pGFP, and 5) US + TMB + pGFP. Next, the 250-kHz transducer was replaced by a 500-kHz spherically focused single-element transducer (H107; Sonic Concepts) with a similar focal depth, and pGFP transfection experiments were repeated at 500 kPa and 500 kHz.

pIFN-β transfection was performed with the NDL cell line. Six groups were tested (n = 4 per group): 1) NTC, 2) TMB + pIFN-β (no US), 3) US + pIFN-β (no TMB), 4) TMB + US, 5) JetPrime transfection agent positive control, and 6) US + TMB + pIFN-β. US was performed with 250 kHz and a PNP of 500 kPa. JetPrime transfection reagents (Polyplus Transfection) were used according to manufacturer's instructions and with the same cell to pIFN-β ratio used with all other treatment conditions.

In Vivo Transfection Studies. A total of 201 bilateral NDL (breast cancer) tumor-bearing mice were studied. All animal-related work performed by our laboratory was in accordance with *Guide for the Care and Use of Laboratory Animals* of the National Institutes of Health (78), and all animal experiments were performed under a protocol approved by the Institutional Animal Care and Use Committee of the University of California, Davis, or Stanford University. All mice in this study were female FVB mice (6 to 9 wk old, 20 to 25 g; Charles River). Mice were orthotopically injected with NDL cells (1×10^6 cells/25 μL of PBS −/−) into the bilateral #4 and #9 inguinal mammary fat pad. Therapy was started when tumors reached ∼4 mm in the largest diameter (∼14 d after cell injections). Due to the capabilities of our current US system, tumors with initial volume between 2 and 120 mm^3 at the start of the study were included. Prior to the transfection experiments, the treated area was shaved and fur further removed using a depilatory cream. US gel was used as a coupling agent. Anesthesia was induced with 2% isoflurane in oxygen (2 L/min). The mouse was positioned on its side, above an agarose spacer (*SI Appendix*, Fig. S17*C*).

Unless otherwise indicated, a center frequency of 250 kHz, PNP of 500 kPa, burst length of 4 ms, pulse repetition frequency of 30 Hz, and a total duration of 3 min were applied. IT injection of a mixture of 2×10^7 in-house made MBs (either antibody or F3-peptide–conjugated TMBs) and 25 μg of the plasmid of choice (final injected volume of less than 25 μL) preceded sonication by 5 min. Injected dose was freshly prepared and injected within 2 min of preparation. The TMB distribution before and after insonation was assessed by US imaging in contrast pulse sequencing contrast mode (Sequoia 512; Siemens; 15L8 transducer; center frequency of 7 MHz) or by a series of coronal images that spanned the tumor diameter at ∼60-μm intervals acquired in nonlinear contrast mode (VisualSonics Vevo 2100; Visualsonics; MS250S transducer; center frequency of 18 MHz).

MB oscillations in vivo were monitored by passive cavitation detection (n = 12 mice) using an unfocused, single-element, 2.25-MHz transducer (V204-RM; Panametrics) with a 3.175-mm aperture. The passive cavitation detection transducer was aligned to the focus of the therapeutic 250-kHz transducer. Received echoes were displayed and post processed using a programmable US system (Verasonics Vantage 256; Verasonics) with the following parameters: sampling frequency of 8.92 MHz, 5,400 recordings for each mouse, and a recording length of 230 μs. To improve the signal-to-noise ratio, a rolling average filter was applied to the spectrograms over five recordings (i.e., 0.167 s). The received spectrograms were normalized to set the 0-dB value as the maximum value based on the first recording at t = 0. Tumor temperature monitoring (n = 11) was accomplished using a 30-gauge needle thermocouple (HYP-1; Omega Engineering), which was placed at the tumor rim with a 1 °C difference assumed between the tumor center and tumor rim. The thermocouple was interfaced to a data acquisition system controlled by LabVIEW (National Instruments).

Three types of plasmids were used for the in vivo transfection studies: pLUC, pGFP, and pIFN-β. For pLUC transfection, five groups of mice were studied: 1) NTC (n = 3); 2) TMB + pLUC (n = 3); 3) US + TMB + pLUC, with a PNP of 200 kPa (n = 3); 4) US + F3 TMB + pLUC with a PNP of 500 kPa (n = 3); and 5) US + antibody-conjugated TMB + pLUC with a PNP of 500 kPa (n = 4). The remaining experiments utilized antibody-conjugated TMB. For pGFP transfection, four groups of mice were studied: 1) NTC (n = 3), 2) TMB + pGFP (n = 3), 3) US + pGFP (n = 3), and 4) US + TMB + pGFP (n = 5). The experiments were repeated three times, at three different time points for flow cytometry (24, 48, and 72 h posttreatment). For pIFN-β transfection, six groups of mice were studied: 1) NTC (n = 6; i.e., 12 tumors), 2) aPD-1 (n = 7; i.e., 14 tumors), 3) US + TMB (n = 3), 4) US + TMB + aPD-1 (n = 6), 5) US + TMB + pIFN-β (n = 4), and 6) US + TMB + pIFN-β + aPD-1 (n = 10). For the survival study, four groups of mice were studied: 1) NTC (n = 3), 2) aPD-1 (n = 3), 3) US + TMB + aPD-1 (n = 6), and 4) US + TMB + pIFN-β + aPD-1 (n = 6). In each case, aPD-1 was injected intraperitoneally at two time points (200 μg, each injection): 3 d prior to and 2 d following US treatment. Treatments were repeated on a weekly basis.

Statistics. Statistical analyses were performed using Prism 8 software (GraphPad Software). Results are presented as mean ± SD, unless otherwise indicated. Statistical tests are reported in the relevant captions. Values of $P < 0.05$ were considered significant and were adjusted for multiple comparisons as indicated in the legends.

Data Availability Statement. All data and scripts discussed in the paper are available to readers at Figshare (https://doi.org/10.6084/m9.figshare.12214364.v2).

ACKNOWLEDGMENTS. This work was supported by National Institutes of Health Grants R01CA112356, R01CA199658, R01CA211602, R01CA210553, R01CA227687, R01EB026094, and Award T32GM007276. This project was supported by the University of California, Davis, Flow Cytometry Shared

Resource Laboratory with funding from National Cancer Institute Grant P30 CA093373 (Cancer Center) and NIH National Center for Research Resources Grant C06-RR12088, with technical assistance from Ms. Bridget McLaughlin and Mr. Jonathan Van Dyke. The content is solely the responsibility of the authors and does not necessarily represent the official view of the National Institutes of Health.

1. A. C. Huang *et al.*, T-cell invigoration to tumour burden ratio associated with anti-PD-1 response. *Nature* **545**, 60–65 (2017).
2. T. F. Gajewski, The next hurdle in cancer immunotherapy: Overcoming the non-T-cell-inflamed tumor microenvironment. *Semin. Oncol.* **42**, 663–671 (2015).
3. J.-M. Escoffre, A. Zeghimi, A. Novell, A. Bouakaz, In-vivo gene delivery by sonoporation: Recent progress and prospects. *Curr. Gene Ther.* **13**, 2–14 (2013).
4. Y. Negishi, Y. Endo-Takahashi, K. Maruyama, Gene delivery systems by the combination of lipid bubbles and ultrasound. *Drug Discov. Ther.* **10**, 248–255 (2016).
5. A. Delalande *et al.*, Cationic gas-filled microbubbles for ultrasound-based nucleic acids delivery. *Biosci. Rep.* **37**, BSR20160619 (2017).
6. A. Le Bon *et al.*, Type I interferons potently enhance humoral immunity and can promote isotype switching by stimulating dendritic cells in vivo. *Immunity* **14**, 461–470 (2001).
7. F. S. Collins, S. Gottlieb, The next phase of human gene-therapy oversight. *N. Engl. J. Med.* **379**, 1393–1395 (2018).
8. P. Zarogoulidis *et al.*, Suicide gene therapy for cancer—current strategies. *J. Genet. Syndr. Gene Ther.* **4**, 1–29 (2013).
9. S. L. Ginn, A. K. Amaya, I. E. Alexander, M. Edelstein, M. R. Abedi, Gene therapy clinical trials worldwide to 2017: An update. *J. Gene Med.* **20**, e3015 (2018).
10. C. E. Thomas, A. Ehrhardt, M. A. Kay, Progress and problems with the use of viral vectors for gene therapy. *Nat. Rev. Genet.* **4**, 346–358 (2003).
11. C. S. Manno *et al.*, Successful transduction of liver in hemophilia by AAV-factor IX and limitations imposed by the host immune response. *Nat. Med.* **12**, 342–347 (2006). Correction in: *Nat. Med.* **12**, 592 (2006).
12. E. Hudry, L. H. Vandenberghe, Therapeutic AAV gene transfer to the nervous system: A clinical reality. *Neuron* **101**, 839–862 (2019).
13. A. Delalande, S. Kotopoulis, M. Postema, P. Midoux, C. Pichon, Sonoporation: Mechanistic insights and ongoing challenges for gene transfer. *Gene* **525**, 191–199 (2013).
14. P. Midoux, C. Pichon, J.-J. Yaouanc, P.-A. Jaffrès, Chemical vectors for gene delivery: A current review on polymers, peptides and lipids containing histidine or imidazole as nucleic acids carriers. *Br. J. Pharmacol.* **157**, 166–178 (2009).
15. J. C. Weaver, Y. A. Chizmadzhev, Theory of electroporation: A review. *Bioelectrochem. Bioenerg.* **41**, 135–160 (1996).
16. E. L. Ayuni *et al.*, In vivo electroporation mediated gene delivery to the beating heart. *PLoS One* **5**, e14467 (2010).
17. A. van Wamel, A. Bouakaz, M. Versluis, N. de Jong, Micromanipulation of endothelial cells: Ultrasound-microbubble-cell interaction. *Ultrasound Med. Biol.* **30**, 1255–1258 (2004).
18. A. van Wamel *et al.*, Vibrating microbubbles poking individual cells: Drug transfer into cells via sonoporation. *J. Control. Release* **112**, 149–155 (2006).
19. I. Lentacker, I. De Cock, R. Deckers, S. C. De Smedt, C. T. W. Moonen, Understanding ultrasound induced sonoporation: Definitions and underlying mechanisms. *Adv. Drug Deliv. Rev.* **72**, 49–64 (2014).
20. Y. Z. Zhao *et al.*, Phospholipids-based microbubbles sonoporation pore size and reseal of cell membrane cultured in vitro. *J. Drug Target.* **16**, 18–25 (2008).
21. M. Shimamura *et al.*, Development of efficient plasmid DNA transfer into adult rat central nervous system using microbubble-enhanced ultrasound. *Gene Ther.* **11**, 1532–1539 (2004).
22. D. Takeuchi *et al.*, Alleviation of Abeta-induced cognitive impairment by ultrasound-mediated gene transfer of HGF in a mouse model. *Gene Ther.* **15**, 561–571 (2008).
23. C. H. Miao *et al.*, Ultrasound enhances gene delivery of human factor IX plasmid. *Hum. Gene Ther.* **16**, 893–905 (2005).
24. S. Chen *et al.*, Efficient gene delivery to pancreatic islets with ultrasonic microbubble destruction technology. *Proc. Natl. Acad. Sci. U.S.A.* **103**, 8469–8474 (2006).
25. J. A. Wolff *et al.*, Direct gene transfer into mouse muscle in vivo. *Science* **247**, 1465–1468 (1990).
26. Y. Taniyama *et al.*, Development of safe and efficient novel nonviral gene transfer using ultrasound: Enhancement of transfection efficiency of naked plasmid DNA in skeletal muscle. *Gene Ther.* **9**, 372–380 (2002).
27. G. Shapiro *et al.*, Multiparameter evaluation of in vivo gene delivery using ultrasound-guided, microbubble-enhanced sonoporation. *J. Control. Release* **223**, 157–164 (2016).
28. A. Delalande, M. F. Bureau, P. Midoux, A. Bouakaz, C. Pichon, Ultrasound-assisted microbubbles gene transfer in tendons for gene therapy. *Ultrasonics* **50**, 269–272 (2010).
29. A. Lawrie *et al.*, Microbubble-enhanced ultrasound for vascular gene delivery. *Gene Ther.* **7**, 2023–2027 (2000).
30. I. Skachkov, Y. Luan, A. F. W. van der Steen, N. de Jong, K. Kooiman, Targeted microbubble mediated sonoporation of endothelial cells in vivo. *IEEE Trans. Ultrason. Ferroelectr. Freq. Control* **61**, 1661–1667 (2014).
31. M. Bez *et al.*, In situ bone tissue engineering via ultrasound-mediated gene delivery to endogenous progenitor cells in mini-pigs. *Sci. Transl. Med.* **9**, eaal3128 (2017).
32. M. Bez *et al.*, Nonviral ultrasound-mediated gene delivery in small and large animal models. *Nat. Protoc.* **14**, 1015–1026 (2019).
33. M. Bez *et al.*, Ultrasound-mediated gene delivery enhances tendon allograft integration in mini-pig ligament reconstruction. *Mol. Ther.* **26**, 1746–1755 (2018).
34. H. Leong-Poi *et al.*, Therapeutic arteriogenesis by ultrasound-mediated VEGF165 plasmid gene delivery to chronically ischemic skeletal muscle. *Circ. Res.* **101**, 295–303 (2007).
35. N. Nomikou, A. P. McHale, Exploiting ultrasound-mediated effects in delivering targeted, site-specific cancer therapy. *Cancer Lett.* **296**, 133–143 (2010).
36. O. Couture, J. Foley, N. Kassell, B. Larrat, J.-F. Aubry, Review of ultrasound mediated drug delivery for cancer treatment: Updates from pre-clinical studies. *Transl. Cancer Res.* **3**, 494–511 (2014).
37. C. Hidai, H. Kitano, Nonviral gene therapy for cancer: A review. *Diseases* **6**, 57 (2018).
38. K.-C. Tsai *et al.*, Differences in gene expression between sonoporation in tumor and in muscle. *J. Gene Med.* **11**, 933–940 (2009).
39. D. L. Miller, S. Bao, R. A. Gies, B. D. Thrall, Ultrasonic enhancement of gene transfection in murine melanoma tumors. *Ultrasound Med. Biol.* **25**, 1425–1430 (1999).
40. D. L. Miller, J. Song, Tumor growth reduction and DNA transfer by cavitation-enhanced high-intensity focused ultrasound in vivo. *Ultrasound Med. Biol.* **29**, 887–893 (2003).
41. K. Iwanaga *et al.*, Local delivery system of cytotoxic agents to tumors by focused sonoporation. *Cancer Gene Ther.* **14**, 354–363 (2007).
42. H. J. Kim, J. F. Greenleaf, R. R. Kinnick, J. T. Bronk, M. E. Bolander, Ultrasound-mediated transfection of mammalian cells. *Hum. Gene Ther.* **7**, 1339–1346 (1996).
43. A. Zeghimi, J. M. Escoffre, A. Bouakaz, Role of endocytosis in sonoporation-mediated membrane permeabilization and uptake of small molecules: A electron microscopy study. *Phys. Biol.* **12**, 066007 (2015).
44. P. Qin, T. Han, A. C. H. Yu, L. Xu, Mechanistic understanding the bioeffects of ultrasound-driven microbubbles to enhance macromolecule delivery. *J. Control. Release* **272**, 169–181 (2018).
45. K. Kooiman, M. Foppen-Harteveld, A. F. W. van der Steen, N. de Jong, Sonoporation of endothelial cells by vibrating targeted microbubbles. *J. Control. Release* **154**, 35–41 (2011).
46. T. van Rooij *et al.*, Viability of endothelial cells after ultrasound-mediated sonoporation: Influence of targeting, oscillation, and displacement of microbubbles. *J. Control. Release* **238**, 197–211 (2016).
47. B. D. M. Meijering *et al.*, Ultrasound and microbubble-targeted delivery of macromolecules is regulated by induction of endocytosis and pore formation. *Circ. Res.* **104**, 679–687 (2009).
48. E. Arkhangelsky, Y. Sefi, B. Hajaj, G. Rothenberg, V. Gitis, Kinetics and mechanism of plasmid DNA penetration through nanopores. *J. Membr. Sci.* **371**, 45–51 (2011).
49. K. Hynynen, F. A. Jolesz, Demonstration of potential noninvasive ultrasound brain therapy through an intact skull. *Ultrasound Med. Biol.* **24**, 275–283 (1998).
50. N. Lipsman *et al.*, Blood-brain barrier opening in Alzheimer's disease using MR-guided focused ultrasound. *Nat. Commun.* **9**, 2336 (2018).
51. S. Qin, K. W. Ferrara, The natural frequency of nonlinear oscillation of ultrasound contrast agents in microvessels. *Ultrasound Med. Biol.* **33**, 1140–1148 (2007).
52. E. A. Neppiras, B. E. Noltingk, Cavitation produced by ultrasonics: Theoretical conditions for the onset of cavitation. *Proc. Phys. Soc. B* **64**, 1032–1038 (1951).
53. L. G. Leal, Bubble dynamics in time-periodic straining flows. *J. Fluid Mech.* **218**, 41–69 (1990).
54. K. B. Bader, C. K. Holland, Gauging the likelihood of stable cavitation from ultrasound contrast agents. *Phys. Med. Biol.* **58**, 127–144 (2013).
55. T. Ilovitsh *et al.*, Enhanced microbubble contrast agent oscillation following 250 kHz insonation. *Sci. Rep.* **8**, 16347 (2018).
56. S. Zhao, K. W. Ferrara, P. A. Dayton, Asymmetric oscillation of adherent targeted ultrasound contrast agents. *Appl. Phys. Lett.* **87**, 1341031–1341033 (2005).
57. S. Zhao, D. E. Kruse, K. W. Ferrara, P. A. Dayton, Selective imaging of adherent targeted ultrasound contrast agents. *Phys. Med. Biol.* **52**, 2055–2072 (2007).
58. S. Zhao, D. E. Kruse, K. W. Ferrara, P. A. Dayton, Acoustic response from adherent targeted contrast agents. *J. Acoust. Soc. Am.* **120**, EL63–EL69 (2006).
59. M. T. Silvestrini *et al.*, Priming is key to effective incorporation of image-guided thermal ablation into immunotherapy protocols. *JCI Insight* **2**, e90521 (2017).
60. M. Chavez *et al.*, Distinct immune signatures in directly treated and distant tumors result from TLR adjuvants and focal ablation. *Theranostics* **8**, 3611–3628 (2018).
61. Y. Sakakima *et al.*, Gene therapy for hepatocellular carcinoma using sonoporation enhanced by contrast agents. *Cancer Gene Ther.* **12**, 884–889 (2005).
62. K. Yamaguchi *et al.*, Ultrasound-mediated interferon β gene transfection inhibits growth of malignant melanoma. *Biochem. Biophys. Res. Commun.* **411**, 137–142 (2011).
63. A. Kheirolomoom *et al.*, Combining activatable nanodelivery with immunotherapy in a murine breast cancer model. *J. Control. Release* **303**, 42–54 (2019).

64. C. Vanpouille-Box *et al*., DNA exonuclease Trex1 regulates radiotherapy-induced tumour immunogenicity. *Nat. Commun.* **8**, 15618 (2017).
65. N. Kopitar-Jerala, The role of interferons in inflammation and inflammasome activation. *Front. Immunol.* **8**, 873 (2017).
66. C. F. Caskey, S. M. Stieger, S. Qin, P. A. Dayton, K. W. Ferrara, Direct observations of ultrasound microbubble contrast agent interaction with the microvessel wall. *J. Acoust. Soc. Am.* **122**, 1191–1200 (2007).
67. F. Petronzelli *et al*., Therapeutic use of avidin is not hampered by antiavidin antibodies in humans. *Cancer Biother. Radiopharm.* **25**, 563–570 (2010).
68. J. Macdonald *et al*., EpCAM immunotherapy versus specific targeted delivery of drugs. *Cancers (Basel)* **10**, 1–13 (2018).
69. J. S. Yeh *et al*., A targeting microbubble for ultrasound molecular imaging. *PLoS One* **10**, e0129681 (2015).
70. H. Zhang *et al*., In vitro characterization and in vivo ultrasound molecular imaging of nucleolin-targeted microbubbles. *Biomaterials* **118**, 63–73 (2017).
71. A. Marabelle *et al*., Starting the fight in the tumor: Expert recommendations for the development of human intratumoral immunotherapy (HIT-IT). *Ann. Oncol.* **29**, 2163–2174 (2018).
72. L. Milling, Y. Zhang, D. J. Irvine, Delivering safer immunotherapies for cancer. *Adv. Drug Deliv. Rev.* **114**, 79–101 (2017).
73. A. M. Ansari *et al*., Cellular GFP toxicity and immunogenicity: Potential confounders in in vivo cell tracking experiments. *Stem Cell Rev. Rep.* **12**, 553–559 (2016).
74. H. Zhang *et al*., Ultrasound molecular imaging of tumor angiogenesis with a neuropilin-1-targeted microbubble. *Biomaterials* **56**, 104–113 (2015).
75. A. Kheirolomoom *et al*., Acoustically-active microbubbles conjugated to liposomes: Characterization of a proposed drug delivery vehicle. *J. Control. Release* **118**, 275–284 (2007).
76. P. M. Siegel, E. D. Ryan, R. D. Cardiff, W. J. Muller, Elevated expression of activated forms of Neu/ErbB-2 and ErbB-3 are involved in the induction of mammary tumors in transgenic mice: Implications for human breast cancer. *EMBO J.* **18**, 2149–2164 (1999).
77. J. K. Miller *et al*., Suppression of the negative regulator LRIG1 contributes to ErbB2 overexpression in breast cancer. *Cancer Res.* **68**, 8286–8294 (2008).
78. National Research Council, *Guide for the Care and Use of Laboratory Animals* (National Academies Press, Washington, DC, ed. 8, 2011).